Supplementary material for: Classically studied coherent structures only paint a partial picture of wall-bounded turbulence

Andrés Cremades[1*], Sergio Hoyas[2] and Ricardo Vinuesa[1*]

[1*]FLOW, Engineering Mechanics, KTH Royal Institute of Technology, Stockholm, SE-100 44, Sweden.

[2]Instituto Universitario de Matemática Pura y Aplicada, Universitat Politècnica de València, Valencia, 46022, Spain.

*Corresponding author(s). E-mail(s): andrescb@kth.se; rvinuesa@mech.kth.se;

Noise-suppression process in the SHAP-value calculation

The high-importance regions in the flow are calculated using the gradient-SHAP algorithm, based on the expected gradients (EG) [1], which is an additive-feature-attribution method designed based on an extension of the Shapley values to a game with infinite players (Aumann-Shapley values) [2]. However, the EG generates high-frequency spatial noise, as observed in several works [1, 3, 4].

The spatial noise generated by the EG can be seen in the top-left image in the Supplementary Figure 1. This noise is a problem to generate the SHAP structures as it can break and divide them, affecting the percolation and their final identification. Therefore, to reduce this spatial noise, the periodicities of the channel in the streamwise and spanwise directions are exploited. The fields are moved along these directions, and then, the model is used to perform the same predictions subjected to the imposed displacements. A schematic representation of the model can be observed in the left box of Supplementary Figure 2. The selected periodic domain (transparent box) is translated to random positions of the original domain (light green box). Note that periodicity is exploited in this process (transparent yellow boxes).

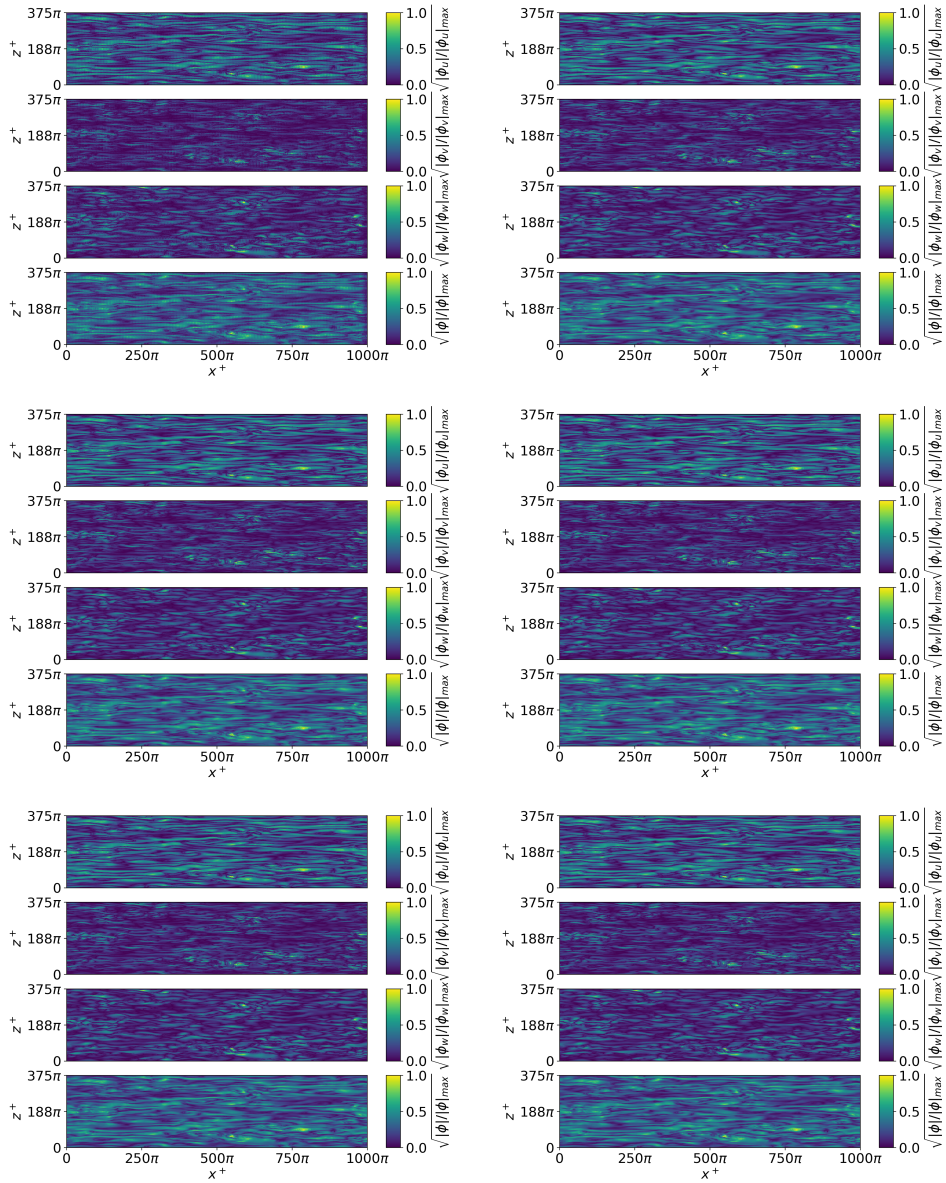

Supplementary Figure 1: **Noise reduction in the SHAP calculation.** Squared root of the instantaneous normalized SHAP-value distribution at $y^+ \approx 12$. From top to bottom, SHAP values of the streamwise ϕ_u, wall-normal ϕ_v and spanwise ϕ_w velocity components, and for the absolute value of the SHAP, $|\phi|$. Computation using single field (top-left), and with 11 (top-right), with 21 (middle-left), with 51 (middle-right), with 101 (bottom-left) and with 201 (bottom-right) translations of the field.

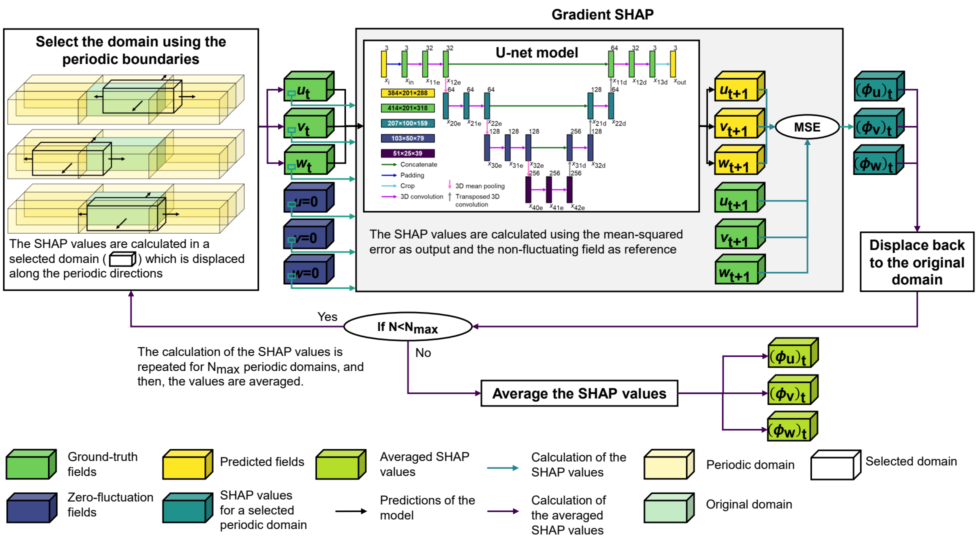

Supplementary Figure 2: **Workflow of the process to remove noise when calculating the SHAP values.** The SHAP values are calculated using the mean-squared error (MSE) of the reconstruction of the model (yellow box) over a selected periodic domain of the input field (green boxes), using a non-fluctuating field (dark blue) as reference. The flow prediction is represented with black flow connections and the SHAP-value calculation with blue flow connections. Then, the SHAP values for a selected periodic domain (blue boxes) are averaged over $N_{\max}$ periodic domains, obtaining the smoothed SHAP values (light green boxes). The selection of the periodic domain and averaging of the SHAP values are presented by the purple flow connections. The selection of the periodic domain is presented in the left box of the figure. The original domain (light green box) is replicated along the periodic boundaries (transparent yellow boxes) and a randomly centered periodic domain (transparent box) is selected for each iteration.

Then, the SHAP values are translated back to the original domain and the results are averaged. The top-right, middle, and bottom images of Figure 1 represent the improvement in the noise reduction as the number of random periodic domains is increased to 11, 21, 51, 101, and 201 translations respectively. Visually, the higher the number of translations, the better the SHAP contours are defined. However, to quantify the noise reduction, the smoothness of the solution is evaluated by calculating the sound-to-noise ratio, SNR, of each field. For this purpose, the three-dimensional fast Fourier transform of the three SHAP components, ψ_n, is calculated:

$$\psi_n\left(\mathcal{X},\mathcal{Y},\mathcal{Z}\right) = \sum_{x=0}^{N_x-1}\sum_{y=0}^{N_y-1}\sum_{z=0}^{N_z-1}\phi_n\left(x,y,z\right)e^{-i2\pi\left(\frac{x\mathcal{X}}{N_x}+\frac{y\mathcal{Y}}{N_y}+\frac{z\mathcal{Z}}{N_z}\right)}, \tag{1}$$

where $\phi_n(x, y, z)$ is the original SHAP value in the spatial domain, $\psi_n(\mathcal{X}, \mathcal{Y}, \mathcal{Z})$ is the Fourier transform in the wavenumber domain and N_x, N_y, N_z are the number of samples in each direction respectively. Then, a low-pass filter is used to suppress wavenumber with a wavelength in the original domain larger than 2 consecutive grid points. The lower wavenumbers are transformed back to the original space using an inverse fast Fourier transform:

$$\phi_n^{LF}(x, y, z) = \frac{1}{N_x N_y N_z} \sum_{x=0}^{N_x-1} \sum_{y=0}^{N_y-1} \sum_{z=0}^{N_z-1} \psi_n^{LF}(\mathcal{X}, \mathcal{Y}, \mathcal{Z}) e^{i2\pi\left(\frac{x\mathcal{X}}{N_x} + \frac{y\mathcal{Y}}{N_y} + \frac{z\mathcal{Z}}{N_z}\right)}, \quad (2)$$

where ϕ_n^{LF} is the low-wavenumber SHAP value field and ψ_n^{LF} its Fourier transform. The noise power of the field is calculated as the difference between the power of ϕ_n and ϕ_n^{LF}:

$$\epsilon^{HF} = \phi_n^2 - \left(\phi_n^{LF}\right)^2. \quad (3)$$

Finally, the signal-to-noise ratio, SNR, is calculated as the ratio of the average value of the signal power and the noise power in decibels:

$$\mathrm{SNR} = 10 \log \frac{\overline{(\psi_n^{LF})^2}}{\overline{\epsilon^{HF}}}. \quad (4)$$

The results of this analysis are presented in Table 1. The table shows the percentage of reconstruction of the least noisy field, obtained after 201 translations, when 1, 11, 21, 51, and 101 translataions were applied. The table evidences that a total number of 11 translations is enough to suppress the high-wavenumber noise of the solution reconstructing more than 97% of the signal for the three SHAP components, with a computational cost of approximately 5% of that of the 201 translations.

Number of translations	$\mathrm{SNR}_{u_i}/\mathrm{SNR}_{u_{201}}$	$\mathrm{SNR}_{v_i}/\mathrm{SNR}_{v_{201}}$	$\mathrm{SNR}_{w_i}/\mathrm{SNR}_{w_{201}}$
1	68.47%	60.62%	63.21%
11	98.02%	97.49%	97.22%
21	98.22%	98.30%	97.63%
51	99.40%	98.93%	99.37%
101	98.54%	98.13%	97.45%

Table 1: **Percentage of reconstruction of the signal-to-noise ratio.** The figure shows the percentage of signal-to-noise ratio reconstruction of the field with 201 translations for 1, 11, 21, 51 and 101 translations.

SHAP structures: additional information

This section shows results complementary to those presented in the main document. The definition of the SHAP structures was defined in the main paper according to a percolation analysis which defines the structure in the regions satisfying:

$$\sqrt{\phi_u^2\left(x,y,z,t\right)+\phi_v^2\left(x,y,z,t\right)+\phi_w^2\left(x,y,z,t\right)} > H\sqrt{\overline{\phi_u^2}\left(y\right)+\overline{\phi_v^2}\left(y\right)+\overline{\phi_w^2}\left(y\right)}. \quad (5)$$

In the previous equation, the SHAP values (importance of the grid points [1, 2]) are defined by the vector $\boldsymbol{\phi} = [\phi_\mathrm{u}, \phi_\mathrm{v}, \phi_\mathrm{w}]$. Each component of the vector links the component of the velocity fluctuation vector $\mathbf{u} = [u, v, w]$ with its impact on the evolution of the flow. In the main text, the fluctuation of the velocity in the streamwise direction of the structures was analyzed for the whole range of wall-normal distances. The following figures show the distribution of the three velocity components for the SHAP structures (Supplementary Figure 3), the Q events or intense Reynolds stress structures [5] (Supplementary Figure 4), the streaks [6] (Supplementary Figure 5) and the vortices [7] (Supplementary Figure 7).

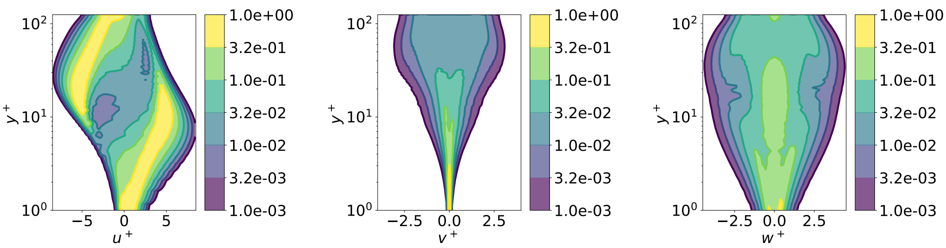

Supplementary Figure 3: **Joint probability density function of the three velocity components of the SHAP structures for the different wall-normal distances.** The figure shows the distribution of the three velocity fluctuations, namely the streamwise, wall-normal, and spanwise components from left to right.

The SHAP structures exhibit a high density in the low-streamwise velocity fluctuation regions for wall-detached structures (ejection-like structures mixing with high-velocity regions) and for high-streamwise velocity fluctuation regions for wall-attached structures (sweep-like structures mixing with low-velocity regions). Furthermore, the wall-normal and spanwise velocities show a symmetric distribution. Most of the regions in the SHAP structures exhibit negligible wall-normal velocity fluctuations and moderate spanwise fluctuations, evidencing a strong correlation between the SHAP structures and the definition of the streaks, which are based on the streamwise and the spanwise fluctuation of the velocity. This agreement between the SHAP structures and the streaks (particularly for $y^+ \simeq 15$) was already introduced in Figure 4 of the main text.

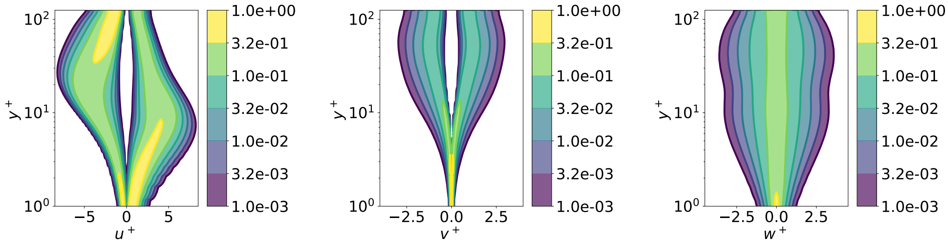

Supplementary Figure 4: **Joint probability density function of the three velocity components of the intense Reynolds stress structures for the different wall-normal distances.** The figure shows the distribution of the three velocity fluctuations, namely the streamwise, wall-normal, and spanwise components from left to right.

Supplementary Figure 4 shows the velocity distribution of the intense Reynolds-stress regions. Most of these structures are located near the wall and exhibit low-velocity fluctuations. Additionally, the sweeps ($u > 0$ and $v < 0$) are found for lower wall-normal distances than the ejections ($u < 0$ and $v > 0$). This is consistent with the previously presented SHAP structures, which point to higher-importance regions where the sweeps enter the higher-local-shear stress regions (near the wall) and when the ejections mix with the lower local-shear-stress regions (far from the wall). In addition, in the main article, the SHAP structures were demonstrated to represent a constant percentage of the Q events. This information, added to the histogram of Supplementary Figure 3, evidences that the important Reynolds-stress structures are those in which the streamwise velocity is important rather than those with a higher wall-normal velocity.

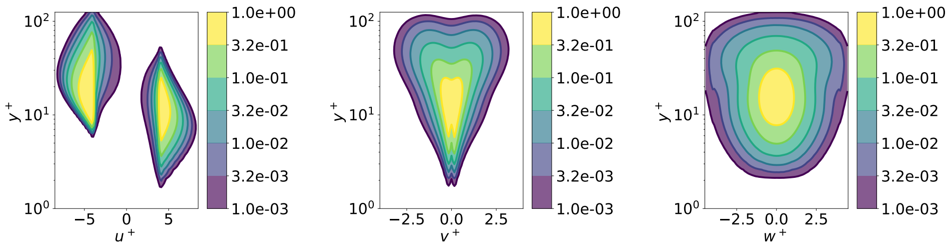

Supplementary Figure 5: **Joint probability density function of the three velocity components of the streaks for the different wall-normal distances.** The figure shows the distribution of the three velocity fluctuations, namely the streamwise, wall-normal, and spanwise components from left to right.

Supplementary Figure 3 shows that the important structures are located near $y^+ \approx 15$. This wall-normal distance matches the distribution of the streaks. In addition, the distribution of the wall-normal and spanwise fluctuations is similar to that of the streaks in Supplementary Figure 5. Therefore, the SHAP structures exhibit a behavior similar to that of the ejection-like structures and sweep-like structures contained in the low- and high-velocity streaks, respectively, which have been identified by Osawa and Jiménez [8] as high-impact regions, and play an important role in turbulence transport.

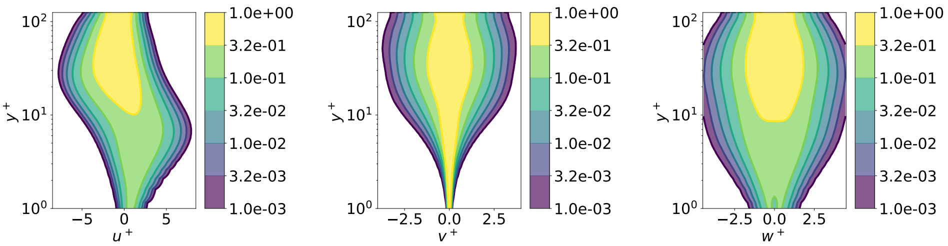

Supplementary Figure 6: **Joint probability density function of the three velocity components of the vortices for the different wall-normal distances.** The figure shows the distribution of the three velocity fluctuations, namely the streamwise, wall-normal, and spanwise components from left to right.

Furthermore, the vortices shown in Supplementary Figure 7 mostly exhibit lower velocity fluctuations for the three components. This fact agrees with the region of the joint probability density function of the SHAP structures (Supplementary Figure 3), where they exhibit a non-negligible probability of structures in regions of low-velocity fluctuations. However, this correlation is not as significant as the agreement with the Q events and the streaks, as discussed in Figure 4 of the main manuscript.

Coincidence between different coherent structures

The percentage of agreement between the SHAP structures and the intense Reynolds-stress structures, streaks and vortices was presented with a visualization of the structures at three different wall-normal distances in Figure 4 from the main paper. This section focuses on extending the visualization of the structures at different wall-normal distances for the whole channel size, Figure 7 and 8.

At $y^+ \approx 3$ most of the SHAP structures are composed by intense Reynolds-stress structures or Q events, with a small presence of streaks and vortices. Nevertheless, there is a large fraction of these Q events that do not match the definition of the SHAP structures. As the wall-normal distance is increased to $y^+ \approx 6$, the streaks gain importance and there is a strong agreement between the SHAP structures and the regions in which Q events and streaks collide; note that this trend can also be observed for $y^+ \approx 34$. Then, for a wall-normal distance $y^+ \approx 13$ the SHAP structures are located inside the streaks, mostly where they match the Q events. For larger wall-normal distances, the SHAP structures are mostly located in regions of intense

Reynolds stress, $y^+ \approx 80$ and $y^+ \approx 109$, and the vortices gain importance as the wall-normal distance increases.

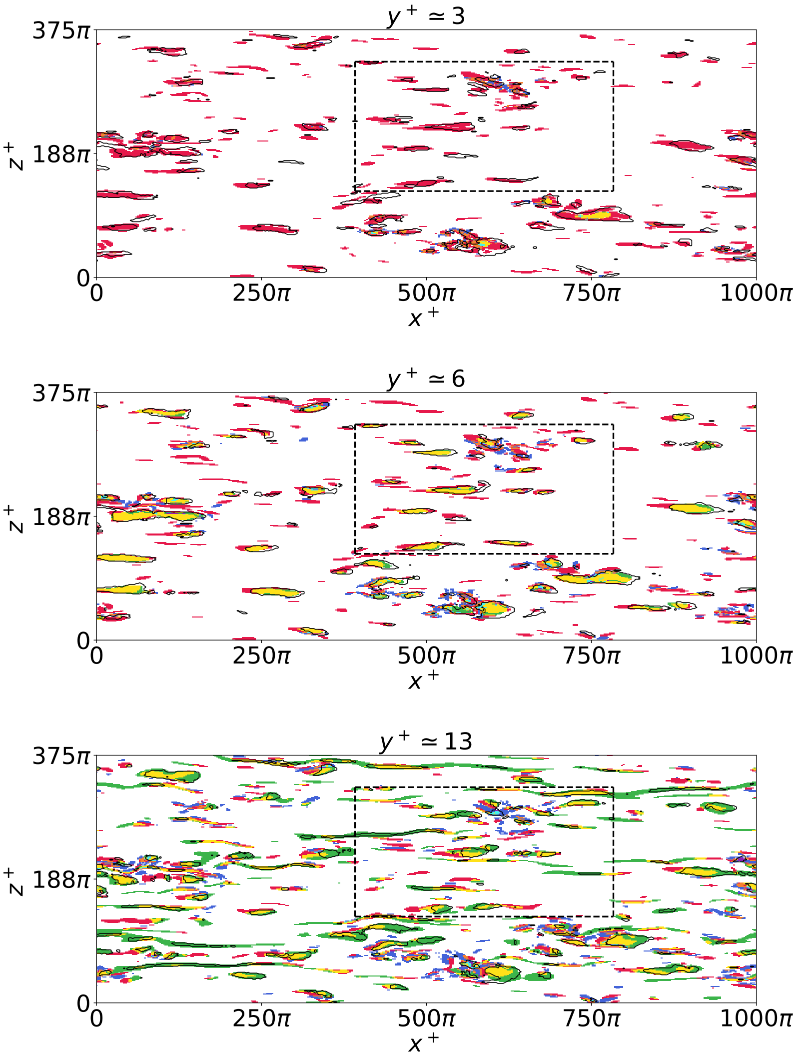

Supplementary Figure 7: Instantaneous coincidence between Q events, streaks, and vortices for six wall-normal locations below $y^+ = 15$. The colors used for the coincidence between structures follow this code: Qs$\setminus$(streaks $\cup$ vortices), streaks$\setminus$(Qs $\cup$ vortices), (Qs $\cup$ streaks)$\setminus$vortices, vortices $\setminus$(Qs $\cup$ streaks), (Qs $\cup$ vortices) $\setminus$streaks, (streaks $\cup$ vortices) $\setminus$Qs, Qs $\cup$ streaks $\cup$ vortices. The SHAP structures are represented by the black solid lines. Note that the dashed lines indicate the domain used in Figure 4 of the main article.

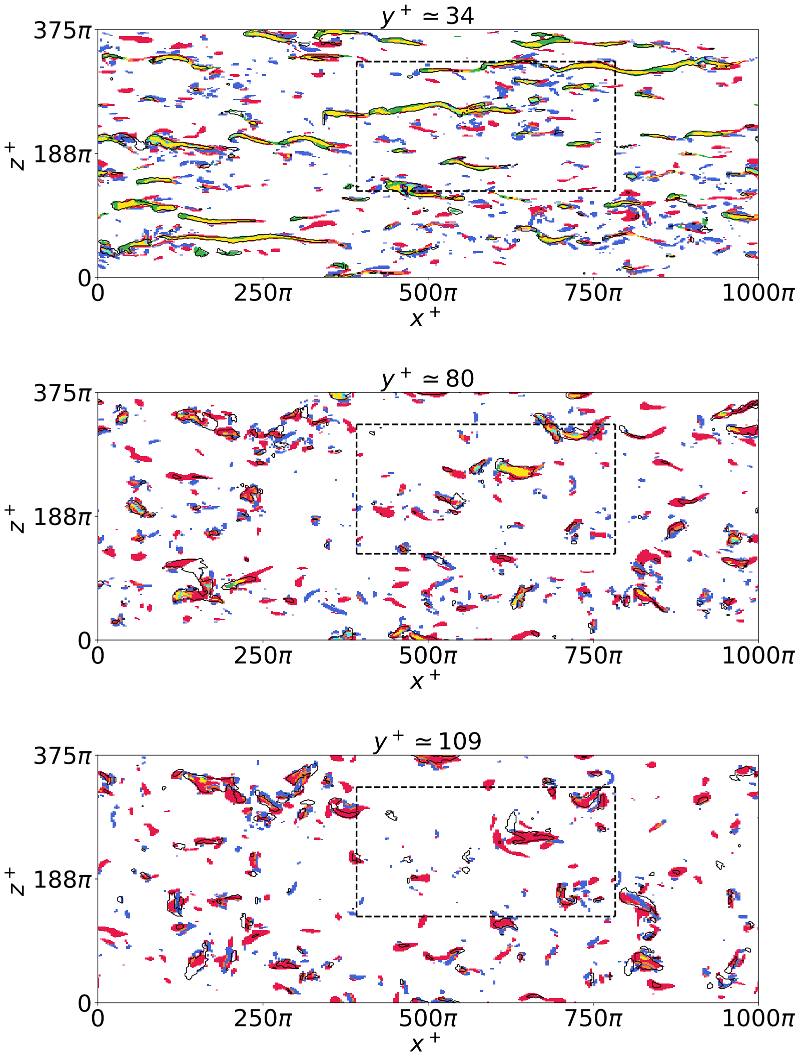

Supplementary Figure 8: Instantaneous coincidence between Q events, streaks, and vortices for three wall-normal locations above $y^+ = 15$. The colors used for the coincidence between structures follow this code: ■ Qs\(streaks ∪ vortices), ■ streaks\(Qs ∪ vortices), ■ (Qs ∪ streaks)\vortices, ■ vortices \(Qs ∪ streaks), ■ (Qs ∪ vortices) \streaks, ■ (streaks ∪ vortices) \Qs, ■ Qs ∪ streaks ∪ vortices. The SHAP structures are represented by the black solid lines. Note that the dashed lines indicate the domain used in Figure 4 of the main article.

Data availability

The minimum representative data used in this study will be made available open access at: https://github.com/KTH-FlowAI. For the complete database, please contact the authors.

Code availability

The codes used for this work will be made available open access at: https://github.com/KTH-FlowAI.

References

[1] Erion, G., Janizek, J.D., Sturmfels, P., Lundberg, S.M., Lee, S.-I.: Improving performance of deep learning models with axiomatic attribution priors and expected gradients. Nature machine intelligence **3**(7), 620–631 (2021)

[2] Lundberg, S.M., Lee, S.-I.: A unified approach to interpreting model predictions. Advances in neural information processing systems **30** (2017)

[3] Rashed-Al-Mahfuz, M., Moni, M.A., Uddin, S., Alyami, S.A., Summers, M.A., Eapen, V.: A deep convolutional neural network method to detect seizures and characteristic frequencies using epileptic electroencephalogram (EEG) data. IEEE journal of translational engineering in health and medicine **9**, 1–12 (2021)

[4] Zheng, Q., Wang, Z., Zhou, J., Lu, J.: Shap-CAM: Visual explanations for convolutional neural networks based on Shapley value. In: European Conference on Computer Vision, pp. 459–474 (2022). Springer

[5] Lozano-Durán, A., Flores, O., Jiménez, J.: The three-dimensional structure of momentum transfer in turbulent channels. Journal of Fluid Mechanics **694**, 100–130 (2012)

[6] Kline, S.J., Reynolds, W.C., Schraub, F.A., Runstadler, P.W.: The structure of turbulent boundary layers. Journal of Fluid Mechanics **30**(4), 741–773 (1967) https://doi.org/10.1017/S0022112067001740

[7] Chong, M.S., Perry, A.E., Cantwell, B.J.: A general classification of three-dimensional flow fields. Journal of Physics A. **2**(5), 765–777 (1990)

[8] Osawa, K., Jiménez, J.: Causal features in turbulent channel flow. arXiv preprint arXiv:2405.15674 (2024)

Acknowledgments

The deep-learning-model training was enabled by resources provided by the National Academic Infrastructure for Supercomputing in Sweden (NAISS) at Berzelius (NSC), partially funded by the Swedish Research Council through grant agreement no. 2022-06725. The data has been obtained with support of grant PID2021-128676OB-I00 funded by MCIN/AEI/10.13039/ 501100011033 and by "ERDF A way of making Europe", by the European Union (SH). RV acknowledges the financial support from ERC grant no. 2021-CoG-101043998, DEEPCONTROL. Views and opinions expressed are however those of the author(s) only and do not necessarily reflect those of the European Union or the European Research Council. Neither the European Union nor the granting authority can be held responsible for them.

Author Contributions

Cremades, A.: Conceptualization, Methodology, Software, Validation, Investigation, Writing - Original Draft, Visualization. Hoyas, S.: Conceptualization, Data curation, resources, Writing - Original Draft, Funding acquisition. Vinuesa, R.: Initial idea, conceptualization, project definition, methodology, resources, Writing - Original Draft, Supervision, Project administration, Funding acquisition.

Competing Interests

The authors declare no competing interests.